PCCP

Hierarchical V4C3TX@NiO-reduced graphene oxide heterostructure hydrogel and defective reduced graphene oxide hydrogel as free-standing anode and cathode for high-performance asymmetric supercapacitor

Journal:	*Physical Chemistry Chemical Physics*
Manuscript ID	CP-ART-02-2023-000595.R1
Article Type:	Paper
Date Submitted by the Author:	05-Mar-2023
Complete List of Authors:	Geng, Ziyu; College of Mathematics & Physics, Beijing University of Chemical Technology, Beijing 100029, China Chen, Weiwen; College of Mathematics & Physics, Beijing University of Chemical Technology, Beijing 100029, China. Qiu, Zenghui; Beijing University of Chemical Technology Xu, Haijun; Beijing University of Chemical Technology Pan, Dingjie; Department of Chemistry and Biochemistry, University of California, 1156 High Street, Santa Cruz, CA, 95064, United States Chen, Shaowei; University of California, Department of Chemistry and Biochemistry

Hierarchical $V_4C_3T_X$@NiO-reduced graphene oxide heterostructure hydrogel and defective reduced graphene oxide hydrogel as free-standing anode and cathode for high-performance asymmetric supercapacitor

Ziyu Geng[a], Weiwen Chen[a,b], Zenghui Qiu[a,b,*], Haijun Xu[a,b,*], Dingjie Pan[c], and Shaowei Chen[c,*]

Asymmetric supercapacitors (ASCs) based on a battery-type anode and a capacitive-type cathode have been attracting extensive interest because of their high energy density. Herein, NiO nanosheets are hydrothermally deposited onto a $V_4C_3T_X$ substrate, which are then assembled into a 3D porous heterostructure hydrogel through a graphene oxide-assisted self-convergence hydrothermal process at low temperatures. The resultant hierarchical $V_4C_3T_X$@NiO-RGO heterostructure hydrogel exhibits an ultrahigh specific capacitance up to 1014.5 F g^{-1} at 1 A g^{-1}. Separately, a defective reduced graphene oxide (DRGO) hydrogel is prepared by a cost-effective hydrothermal procedure followed by cobalt-catalyzed gasification, which shows a higher specific capacitance (258 F g^{-1} at 1 A g^{-1}) than untreated RGO hydrogel (176 F g^{-1}). These two electrodes are then assembled into an ASC, the device features a stable operating voltage of 1.8 V, a maximum energy density of 86.22 Wh kg^{-1} at 900 W kg^{-1}, along with excellent cycling stability at 96.4% capacitance retention after 10,000 cycles at 10 A g^{-1}. Results from this work highlight the unique potential of MXenes-based materials for the construction of high-performance ASCs.

Keywords: MXene; heterostructure; graphene oxide; porous hydrogel; defect engineering; asymmetric supercapacitor

Introduction

Supercapacitors (SCs) have been considered as sustainable electrochemical energy storage devices,[1,2] featuring an ultrahigh power density (10 to 10^4 W kg^{-1}), fast charging/discharging, and excellent cycling stability (cycle life >10^5 cycles), and finding widespread applications in transportation, hybrid batteries, etc.[3-5] One major issue about SCs is the limited energy-storage performance, as compared to batteries.[4-7] This has become a leading topic in recent research. Asymmetrical supercapacitors (ASCs) represent a unique platform to achieve a high energy density.[8]

Based on the energy storage mechanism, SCs can be classified into three different types, electric double-layer capacitors (EDLCs), pseudocapacitors, and ASCs. EDLCs store and release charges at the electrode/electrolyte interface via rapid ion adsorption/desorption, but typically display a low energy density.[9] For pseudocapacitors, energy is stored through a Faradaic process involving fast reversible redox reactions occurring both on the surface and in the interior of the electrode materials. Thus, pseudocapacitive electrodes exhibit a high energy density, but poor cycling stability and low power density.[4-7,10-12] ASCs refer to the devices in which one battery-type electrode acts as the anode while the cathode is a capacitor-type electrode.[3,8] During the charge/discharge processes, ASCs take full advantage of the different potential windows of the two electrodes to maximize the operating voltage. In fact, properly designed ASCs have been recognized as viable devices to achieve both a high energy density and a high power density.

2D transition-metal carbides/nitrides/carbonitrides, MXenes, have been used in various applications since the first synthesis by the Gogotsi group in 2011.[13-16] Typically, the production of MXenes involves selective etching of the "A" element from the ternary layered MAX phases with a general formula of $M_{n+1}AX_n$ in a hydrofluoric acid-containing solution. The resulting single MXene sheets consist of 3, 5, 7 or 9 atomic layers for M_2X, M_3X_2, M_4X_3, and M_5X_4,[13, 17] with a general composition of $M_{n+1}X_nT_X$, where T_X is surface functional groups and determines the hydrophilicity of the materials.[18] It is well-known that the abundant oxidation valence states of transition metals can significantly enhance the intrinsic pseudocapacitance of MXene-based electrodes.[19] For instance, V-based MXene $V_4C_3T_X$ has been used as high-performance SC electrodes because of various valence states of the vanadium element ranging from +2 to +5.[20] Multi-layered $V_4C_3T_X$ also possesses a larger

[a] College of Mathematics & Physics, Beijing University of Chemical Technology, Beijing 100029, China
[b] Beijing Bioprocess Key Laboratory, Beijing University of Chemical Technology, Beijing 100029, China
[c] Department of Chemistry and Biochemistry, University of California, 1156 High Street, Santa Cruz, CA, 95064, United States
* E-mail: zhqiu@buct.edu.cn (Z.H.Q.), hjxu@buct.edu.cn (H.J.X.), and shaowei@ucsc.edu (S.W.C.)

interlayer spacing than Ti-based MXenes, which is favorable to the intercalation and deintercalation in energy storage.[21] In fact, owing to the high electrical conductivity, adjustable layer spacing, and rich redox active sites, $V_4C_3T_X$ electrodes have been found to display a high-rate performance, high power density and high energy density.[22]

Nevertheless, there are two major challenges when raw $V_4C_3T_X$ is used as electrodes for high-energy SCs. First, the surface functional groups and surface defects formed in the etching process may negatively influence the energy-storage property, and compromise the theoretical specific capacity.[20, 23] Second, as a typical 2D nanomaterial, the strong van der Waals interactions between adjacent $V_4C_3T_X$ nanosheets can lead to self-restacking, and significantly limit the full utilization of the active surface area.[18,24] To improve the specific capacitance of $V_4C_3T_X$, one effective strategy is to fabricate $V_4C_3T_X$-based heterostructures that combine the advantages of $V_4C_3T_X$ with pseudocapacitive materials.[24-26] The unique 2D lamellar structure and abundant terminal functional groups/atomic defects of $V_4C_3T_X$ render it possible to construct desired synergetic heterostructures with high structural stability.[20] The obtained heterostructures can not only strengthen the individual properties of each constituent, but also exhibit a synergistic effect of high reactivity, ultrahigh specific capacitance and superb electrical conductivity.[26] For example, NiO features a stable structure, high theoretical specific capacity (3750 F g^{-1}) and low cost, and is hailed as a powerful candidate to combine with $V_4C_3T_X$ to form heterostructures with a face-to-face contact of both components.[27] To mitigate the issue of aggregation, one viable way is to integrate the layered $V_4C_3T_X$@NiO heterostructure into a 3D interlinked structure,[28,29] which can also provide abundant active sites and fast ions/electron transport channels to effectively boost the electrochemical reaction kinetics.[30] Moreover, the disordered structure formed from the macroscopic interlinked framework can slightly inhibit structural expansion during the repetitive charge/discharge, leading to excellent electrochemical stability.

Experimentally, the self-gelation of reduced graphene oxide (RGO) leads to the formation of 3D mesoporous hydrogels that can be composited with various active materials to produce SC electrodes, which can be exploited for the preparation of $V_4C_3T_X$@NiO-RGO heterostructure hydrogels.[29-3129,31-33] Owing to the synergistic effect among each components and the porous interconnected architecture, the resultant 3D hierarchical $V_4C_3T_X$@NiO-RGO hydrogels not only take both merits of outstanding electrical conductivity and high specific capacitance, but also obviously avoid the aggregation and significantly increase the surface utilization, indicating the 3D hierarchical $V_4C_3T_X$@NiO-RGO heterostructure hydrogel with improved overall electrochemical performance can be used as a competitive anode for ASCs.

Carbon-based materials have been widely employed as ASC cathodes,[34] most notably graphene which features excellent electrochemical stability, high electrical conductivity, and large specific surface area.[35] However, aggregation of graphene nanosheets and the intrinsically narrow ion/electron transport channels lead to degradation of the capacitance characteristics. Defect engineering has been recognized as an effective strategy to enhance the storage properties, in particular, for ASC cathode materials.[36] This can be achieved by, for instance, patterning on graphene surfaces to form mesoporous structures, which provides abundant pathways for ion penetration into the materials, leading to improved storage performance.[37] In comparison to patterning methods like electron plasma etching and lithography that involve high temperatures and dangerous gas atmospheres, carbon gasification catalyzed by metallic and oxide particles in a controlled atmosphere has emerged as a eco-friendly method suitable for large-scale preparation.[38,39] To prevent aggregation, the obtained defective RGO (DRGO) can be assembled into interconnected frameworks due to self-gelation of RGO produced by the reduction of GO with L-ascorbic acid.[40] The resultant 3D DRGO hydrogels with mesopore structure not only provide abundant pathways for speedy ionic/electron diffusion, but also obviously avoid the aggregation and increase the surface utilization of DRGO, leading to improved storage performance.

In this work, 3D hierarchical $V_4C_3T_X$@NiO-RGO heterostructure hydrogels are fabricated by an efficient, two-step procedure and used as the anode for ASCs. In the first step, $V_4C_3T_X$@NiO heterostructures are prepared by a chemical bath deposition and thermal annealing process, and incorporated into the conductive, porous hydrogels via a low-temperature GO-assisted self-convergence hydrothermal strategy. DRGO hydrogels are prepared and used as a cathode for ASCs. DRGO hydrogels are prepared via the GO self-gelation hydrothermal strategy with L-ascorbic acid as the reducing agent, in conjunction with cobalt-catalyzed gasification. Due to the excellent mechanical property of the hydrogels, the materials are used directly without binders as the ASC anode and cathode. The free-standing $V_4C_3T_X$@NiO-RGO//DRGO ASC device reaches a maximum operating voltage of 1.8 V, a maximum energy density of 86.22 Wh kg^{-1} at 900 W kg^{-1} and excellent cycle stability (retention of 96.4% capacitance over 10,000 cycles).

Experimental section

Preparation of delaminated $V_4C_3T_X$ MXene

High-quality $V_4C_3T_X$ was synthesized by following a classical etching method where the Al layers were selectively etched from V_4AlC_3 MAX-phase precursor (<38 μm).[20] Typically, 1 g of LiF was dissolved in 20 mL of a 9 M HCl solution, into which was slowly added 1 g of Ti_3AlC_2 powders under stirring for 30 min in an ice bath and then heated at 40 °C for 36 h.[22] The resultant clay-like $V_4C_3T_X$ suspension was centrifuged at 3500 rpm and washed repeatedly with deionized (DI) water and absolute alcohol until pH ≥ 6. A homogeneous dispersion of delaminated $V_4C_3T_X$ was then prepared by ultrasonication of the above product under an Ar flow followed by centrifugation (3500 rpm) for 1 h. Finally, the dark green supernatant was collected and freeze-dried to obtain few-layer $V_4C_3T_X$ floccules.

Fabrication of $V_4C_3T_X$@NiO heterostructures

$V_4C_3T_X$@NiO heterostructures were fabricated by liquid phase deposition along with thermal annealing. Typically, 1 g of the $V_4C_3T_X$ prepared above was added into a 400 mL solution containing 3.88 g of $Ni(NO_3)_2{\cdot}6H_2O$ and 16.06 g of urea under sonication for 1 h to produce a homogeneous suspension. The mixture was heated in an oil bath at 90 °C for 3 h under magnetic stirring, and the precipitate was aged for 12 h, which was then collected by centrifugation at 10,000 rpm, rinsed with ethanol and DI water for 5-6 times, and freeze-dried. This precursor was converted into $V_4C_3T_X$@NiO heterostructures by thermal annealing at 350 °C for 2 h at a slow heating rate of 2 °C min^{-1}. As a comparison, pure NiO was also produced in the same method but in the absence of $V_4C_3T_X$.

Synthesis of $V_4C_3T_X$@NiO-RGO hydrogel

The synthesis of 3D $V_4C_3T_X$@NiO-RGO hydrogel was based on a GO-assisted self-convergence hydrothermal strategy. GO was fabricated from natural graphite flakes by an improved Hummers' method.[41] A GO homogeneous colloidal suspension (2 mg mL^{-1}) was prepared by ultrasonication of GO in DI water for 4 h, followed by centrifugation (3800 rpm for 30 min) to remove thick layers. 8 mg of $V_4C_3T_X$@NiO powders was then added into a 15 mL glass vial containing 1 mL of the prepared GO colloidal suspension under mechanical stirring and ultrasonic dispersion for 1 h each to obtain a homogeneous suspension, into which was immediately added 4 mg of L-ascorbic acid (L-ascorbic acid/GO = 2:1, w/w) under magnetic stirring for 30 min. The vessel was then sealed and underwent a hydrothermal treatment for 5 h at 90 °C, affording $V_4C_3T_X$@NiO-RGO hydrogel that was rinsed with DI water several times until pH was around 7. For comparison, RGO hydrogel was also fabricated by the same process but without the addition of $V_4C_3T_X$@NiO heterostructures.

Preparation of DRGO and RGO hydrogels

DRGO hydrogel was prepared via an efficient and environmentally friendly hydrothermal method followed by cobalt (Co) catalyzed gasification in ambient. Firstly, a certain amount of Co particles was diffused into 1 mL of the prepared GO colloidal suspension (2 mg mL^{-1}) under mechanical stirring and ultrasonic dispersion for 1 h each to obtain a homogeneous GO/Co (10 wt%) hybrid solution, into which was added 4 mg of L-ascorbic acid (GO/L-ascorbic acid = 1:2, w/w) under mechanical stirring for 30 min, and the resulting solution was heated hydrothermally at 90 °C for 5 h to obtain an RGO hydrogel with Co particles attached uniformly on the surfaces. The resulting hybrid hydrogel was then rinsed with DI water repeatedly until pH ≈ 7, collected by lyophilization, and underwent oxidation in air at 300 °C for 30 min involving two reactions, (i) $6CoO + O_2 \rightarrow 2Co_3O_4$, and (ii) $Co_3O_4 + C \rightarrow 3CoO + CO$.[38] The product was finalized immersed in a boiled concentrated nitric acid (98 %) for 1 h to remove the remaining cobalt oxide, rinsed with DI water several times and freeze-dried. As a comparison, RGO hydrogel was prepared by the same process but without Co particles.

Material characterization

The morphologies of the samples were examined by field-emission scanning electron microscopy (FESEM, Quant 250 FEG) and transmission electron microscopy (TEM, JEOL JEM-2010F) measurements. Elemental mapping studies based on energy dispersive X-ray analysis (EDX) and selected-area electron diffraction (SAED) were performed with the JEOL 2010F microscope. Crystal structures were characterized by powder X-ray diffraction (XRD) measurements on a BRUKER diffractometer (D8 advance CuKα radiation source, λ = 0.15406 nm), and Raman spectra were acquired with a Renishaw in Via micro-Raman system (Thermo Fischer DXR) with a He-Ne laser beam at the excitation wavelength of 532 nm. X-ray photoelectron spectroscopy (XPS) measurements was performed with a Kratos-Axis spectrometer through a monochromatic Al K_α (1486.6 eV) X-ray source (15 kV and 10 mA) and a hemispherical electron energy analyzer. Specific surface area was calculated through the Brunauer–Emmett–Teller (BET) method, and pore size distribution curves were assessed through the Barrett-Joyner-Halenda (BJH) model from the adsorption branch of the isotherms.

Electrochemical measurements

The electrochemical behaviors of the as-prepared electrodes were examined in a typical three-electrode system in 1 M KOH, in which a Pt foil was used as the counter electrode, and an Hg/HgO electrode as the reference electrode. The $V_4C_3T_X$ or $V_4C_3T_X$@NiO heterostructures were used as the active materials on the working electrode, which was prepared by pressing a homogeneous slurry containing 80 wt% of active materials, 10 wt% of carbon black, and 10 wt% of polytetrafluoroethylene (PTFE), along with a small amount of anhydrous ethanol onto a nickel foam current collector (1 cm × 1 cm, under a pressure of 10 MPa). Owing to the excellent mechanical property, the 3D RGO, DRGO, and $V_4C_3T_X$@NiO-RGO hydrogel working electrodes were fabricated without binders. The mass of the active materials in each electrode was ca. 1.0 mg. After being dried at 90 °C for 12 h in a vacuum oven, the working electrode was immersed in a 1 M KOH solution for 24 h to ensure equilibrium contact between the active materials and electrolyte. All electrochemical tests, including cyclic voltammetry (CV), electrochemical impedance spectroscopy (EIS), and galvanostatic charge-discharge (GCD), were undertaken with a CHI 660B electrochemical workstation. In addition, the specific capacitance (C_S, F g^{-1}) of the active materials on the working electrode was calculated from the GCD curves based on the equation of $C_S = I\Delta t/m\Delta V$, where I (A) is the discharge current, Δt (s) is discharge time, m (g) is the mass loading of active material on the working electrode, and ΔV (V) represents a potential window.

Assembly and electrochemical tests of ASC

The $V_4C_3T_X$@NiO-RGO//DRGO ASC was assembled by using $V_4C_3T_X$@NiO-RGO hydrogel as the anode and DRGO hydrogel as the cathode in a 1 M KOH electrolyte, and the electrochemical measurements of the ASC were carried out in a three-electrode system. The optimal mass ratio of $V_4C_3T_X$@NiO-RGO and DRGO was calculated by balancing the charge between the anode and cathode, $Q = C\Delta Vm$; $Q_+ = Q_-$, $m_+/m_- = C_-\Delta V_-/C_+\Delta V_+$,[42] where Q_+ and Q_- refer to the charge stored at the anode and cathode, C_+ and C_- are the specific capacitance of the anode and cathode in

three-electrode system, ΔV_+ and ΔV_- represent the potential window, and m_+ and m_- stand for the active material mass in the anode and cathode, respectively. Furthermore, the energy density (E, Wh kg^{-1}) and power density (P, W kg^{-1}) of the ASC were calculated by $E = C_{ASC}\Delta V^2/7.2$ and $P = 3600E/\Delta t_S$, where C_{ASC} (F g^{-1}) and ΔV (V) stand for the specific capacitance and the potential window of the ASC, respectively, and Δt_S (V) represents the discharge time of the ASC.

Results and discussion

Structure and electrochemical characteristics of anode materials

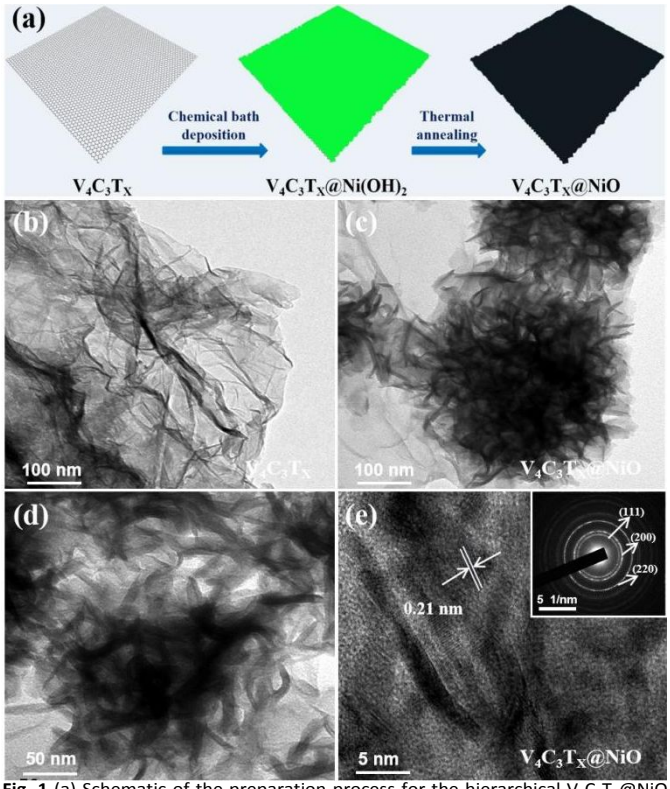

Fig. 1 (a) Schematic of the preparation process for the hierarchical $V_4C_3T_X$@NiO core-shell heterostructure. Typical TEM images of (b) $V_4C_3T_X$, (c, d) $V_4C_3T_X$@NiO. (e) Representative HRTEM image of $V_4C_3T_X$@NiO, with a scale bar of 5 nm. Inset is the corresponding SAED patterns.

Fig. 1a shows the synthesis process for the hierarchical $V_4C_3T_X$@NiO core-shell heterostructure, where ultrathin $Ni(OH)_2$ nanosheets were uniformly deposited onto the $V_4C_3T_X$ surface by chemical bath deposition, and the resultant $V_4C_3T_X$@$Ni(OH)_2$ was thermally annealed in air to produce hierarchical $V_4C_3T_X$@NiO heterostructures. The morphologic structures of the prepared samples were firstly characterized by TEM measurements. As shown in Fig. 1b, the $V_4C_3T_X$ nanosheets exhibit a two-dimensional wrinkled paper-like structure. Fig. 1c-d display that the $V_4C_3T_X$@NiO heterostructure consisted of a hierarchical structure with the $V_4C_3T_X$ surface uniformly covered with few-layer ultrathin NiO films. In high-resolution TEM measurements (Fig. 1e), the NiO nanosheets can be seen to display distinctly clear lattice fringes with an interplanar spacing of about 0.21 nm, consistent with the NiO (200) crystalline planes (JCPDS 43-1477).[27] This is consistent with the SAED patterns (Fig. 1e inset) which show three intense rings due to the (111), (200) and (220) crystal planes of NiO. Moreover, from Fig. 1e it can be seen that the hierarchical $V_4C_3T_X$@NiO heterostructures feature a close face-to-face contact of both components, which can not only provide abundant channels for electrolyte ion transport, but also offer good mechanical strength, leading to excellent electrochemical performance, as observed below.

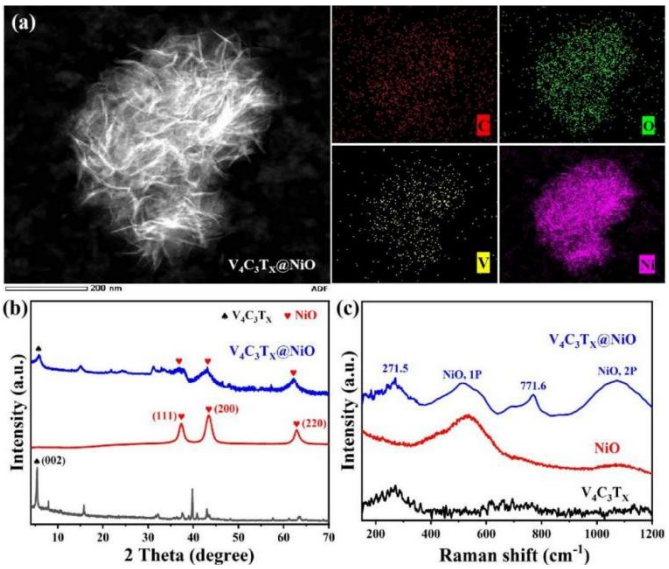

Fig. 2 (a) EDX patterns of $V_4C_3T_X$@NiO heterostructure, with the corresponding elemental maps of C, O, V, and Ni in the $V_4C_3T_X$@NiO heterostructure. (b) XRD patterns and (c) Raman spectra of $V_4C_3T_X$, NiO, and $V_4C_3T_X$@NiO heterostructure.

Further structural insights were obtained in EDX analysis, where the elements of C, Ni, V, and O can be clearly identified in the sample. From the corresponding elemental maps (Fig. 2a), these elements can be observed to distribute rather evenly within the sample, confirming the good combination of flower-like NiO with $V_4C_3T_X$ nanosheets. The phase and crystal structure of the samples were characterized via XRD and Raman measurements. The XRD patterns of the samples are shown in Fig. 2b. The black curve shows one strong peak at $2\theta = 5.41°$ due to the (002) crystal plane of $V_4C_3T_X$.[20] The additional diffraction peaks centered at $2\theta = 37.2°$, 43.2° and 62.8° can be respectively ascribed to the (111), (200), and (220) crystal planes of NiO (JCPDS 43-1477).[27] These characteristic peaks can also be clearly found in the $V_4C_3T_X$@NiO heterostructures; yet, the (002) peak for $V_4C_3T_X$@NiO shifts to a lower angle than that for $V_4C_3T_X$, suggesting deposition of NiO onto the $V_4C_3T_X$ nanosheets inhibits the aggregation of $V_4C_3T_X$. Furthermore, no diffraction peaks can be identified for $Ni(OH)_2$, confirming that the symmetric Ni-OH has been transformed into Ni-O in the thermal annealing process. Consistent results were obtained in Raman measurements. Fig. 2c shows that both $V_4C_3T_X$ and $V_4C_3T_X$@NiO exhibited the characteristic peaks at 271.5 and 771.6 cm^{-1}, corresponding to the vibrations of the V-C bonds of $V_4C_3T_X$[23]. Meanwhile, two broad peaks at 566 cm^{-1} and 1068 cm^{-1}, due respectively to the first-(1P) and second-order phonon (2P) scattering, were clearly observed in the Raman spectra of NiO and $V_4C_3T_X$@NiO heterostructures. The fact that no additional peak is detected confirms that the flower-like NiO nanosheets

were uniformly deposited over the entire exposed surface of the $V_4C_3T_X$ nanosheets.

The chemical composition and bonding states of the various elements in the nanocomposites were further analyzed by XPS measurements. From the survey spectra in Fig. 3a and b, four peaks can be identified for $V_4C_3T_X$ and $V_4C_3T_X$@NiO heterostructure at around 285.1, 517.1, 531.5, and 685.7 eV, due to the C 1s, V 2p, O 1s, and F 1s electrons, respectively.[20] A new peak appears at 856 eV corresponding to Ni after the deposition of NiO onto the $V_4C_3T_X$ nanosheets surface, indicating the successful synthesis of the heterostructures (Fig. 1a).[23] Fig. 3c-f depict the high-resolution XPS spectra of the $V_4C_3T_X$@NiO heterostructure. In Fig. 3c, the high-resolution spectrum of C 1s electron can be deconvoluted into five peaks at 282.5, 284.6, 285.3, 286.3, and 288.8 eV, due to C-V, C-C, C-H, C-O and O-C=O, respectively.[21] Fig. 3d displays the V 2p region for $V_4C_3T_X$, where three doublets were deconvoluted, 513.6/521.5 eV to the $2p_{3/2}/2p_{1/2}$ electrons of V-C,[26] 514.9/523.1 eV to V^{3+}, and 516.9/524.6 eV to V^{4+}.[22] The deposition of NiO on the $V_4C_3T_X$ surface led to a decrease of the content of functional groups and partial oxidation. In the O 1s spectra (Fig. 3e), two peaks were resolved at 530.7 (V-O) and 531.9 eV (V-OH), corresponding to the adsorbed H_2O, and another at 529.2 (Ni-O), due to oxygen bonded to Ni.[27] The formation of NiO is observed in the high-resolution scans of the Ni 2p electrons (Fig. 3f), where deconvolution of the spectrum yielded two peaks at 853.7 and 855.6 eV, due to the $2p_{3/2}$ and $2p_{1/2}$ electrons of Ni^{2+}, respectively.[43]

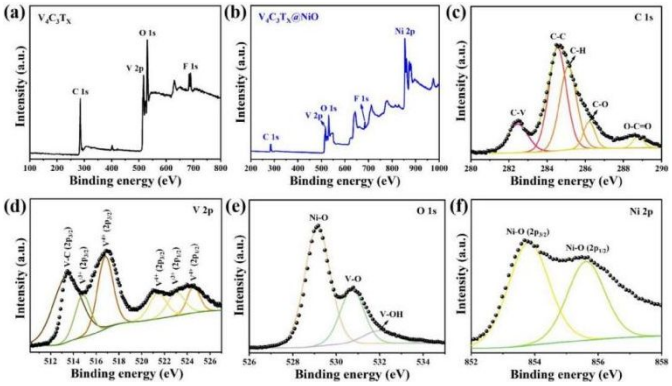

Fig. 3 (a, b) XPS survey spectrum of $V_4C_3T_X$ and $V_4C_3T_X$@NiO heterostructure. High-resolution scans of (c) C 1s, (d) V 2p, (e) O 1s, and (f) Ni 2p electrons of $V_4C_3T_X$@NiO heterostructure.

The fabrication process of $V_4C_3T_X$@NiO-RGO hydrogel by GO-assisted hydrothermal assembly is schematically illustrated in Fig. 4a. To assemble $V_4C_3T_X$@NiO heterostructures into a 3D porous architecture, GO was utilized as the gelation agent. In view of the easy oxidization of $V_4C_3T_X$ nanosheets in water at high temperatures, a mild hydrothermal strategy at low temperatures was selected to avoid severe oxidation and structural degradation of $V_4C_3T_X$. During the hydrothermal assembling process, GO was reduced by both ascorbic acid and surface functional groups of $V_4C_3T_X$ and the resultant RGO nanosheets were interconnected with each other to form a 3D framework, while the $V_4C_3T_X$@NiO were assembled into the macroscopic RGO framework to produce a $V_4C_3T_X$@NiO-RGO heterostructured hydrogel. As shown in Fig. 4b, when the $V_4C_3T_X$@NiO/GO mixed colloid was aged 90 °C, 3D hydrogels with a diameter and a height of about 0.8 and 0.5 cm were formed from the $V_4C_3T_X$@NiO/GO precursor at 80 wt% of $V_4C_3T_X$@NiO.

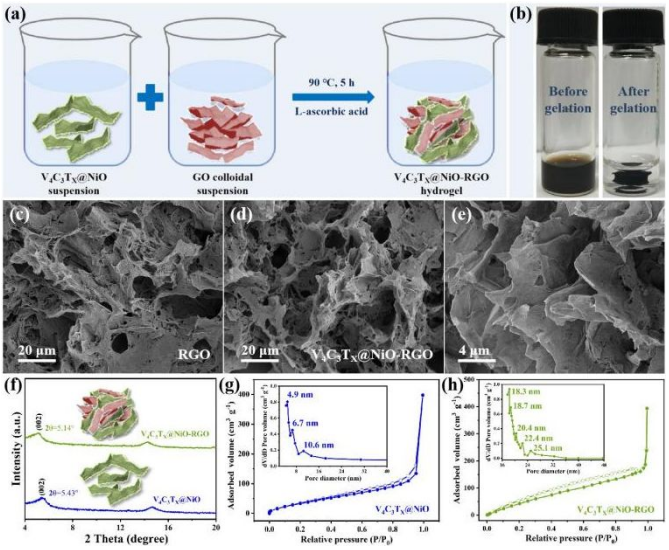

Fig. 4 (a) Schematic illustration of the synthesis process of 3D $V_4C_3T_X$@NiO-RGO heterostructured hydrogel. (b) Photos of a homogeneous $V_4C_3T_X$@NiO/GO colloid before and after reaction at 90 °C. (c) SEM image of RGO hydrogel. (d, e) SEM images of $V_4C_3T_X$@NiO-RGO heterostructured hydrogel. (f) XRD patterns of $V_4C_3T_X$@NiO and $V_4C_3T_X$@NiO-RGO. Typical N_2 adsorption-desorption isotherms of (g) $V_4C_3T_X$@NiO heterostructure and (h) $V_4C_3T_X$@NiO-RGO heterostructured hydrogel.

Fig. 4c-e show the SEM images of the RGO and $V_4C_3T_X$@NiO-RGO foams obtained by freeze-drying the obtained hydrogels, separately. It is observed that the foams featured a continuous and well-defined 3D interconnected porous structure with random open pores and thin pore walls. From the magnified SEM image of the hybrid foam (Fig. 4e), one can see that the heterostructured hydrogel retains the 2D flat structure, and the pore size of the network ranges from sub-micrometers to several micrometers and the pore walls consist of stacked $V_4C_3T_X$@NiO heterostructures crosslinked by RGO nanosheets. This indicates that the 3D hydrogel effectively prevents restacking of $V_4C_3T_X$ nanosheets, which is favorable for the enhancement of performance. From the XRD patterns in Fig. 4f one can see that the (002) diffraction peak shifts from 5.43° for $V_4C_3T_X$@NiO powder to 5.14° for $V_4C_3T_X$@NiO-RGO hydrogel after the intercalation of RGO nanosheets among the $V_4C_3T_X$@NiO layers, corresponding to an enlarged interlayer spacing from 1.29 to 1.71 nm. Moreover, the (002) peak of the hydrogel is broader than that of the powder, suggesting an inhibition of aggregation of $V_4C_3T_X$@NiO nanosheets, which is conducive to enhancing the capacitance in electrochemical applications.

N_2 adsorption−desorption measurements show that the restacking of the $V_4C_3T_X$@NiO heterostructure was effectively restrained. Fig. 4g shows the N_2 adsorption−desorption isotherms of the $V_4C_3T_X$@NiO powders, which possesses a type IV isotherm with a very low adsorption volume in the low and medium relative pressure ranges, suggesting the absence of micropores and mesopores, while the isotherm displays a maximum adsorption capacity at $P/P_0 = 1$, corresponding to micropores responsible for abundant adsorption of N_2 at high

relative pressures. In contrast, the $V_4C_3T_x$@NiO-RGO hydrogel features a type II isotherm with a significant hysteresis loop in the relative pressure range from 0.1 to 1.0 (Fig. 4h), revealing a typical mesoporous structure. The specific surface area of $V_4C_3T_x$@NiO-RGO hydrogel is then estimated to be 315 $m^2 g^{-1}$, which is approximately 4.04 times that of $V_4C_3T_x$@NiO (78 $m^2 g^{-1}$). Additionally, the pore size is calculated by the BJH method. From the inset to Fig. 4g, one can see that $V_4C_3T_x$@NiO powder consisted mainly of micropores with an average pore size of 4.9, 6.7, and 10.6 nm, while, the $V_4C_3T_x$@NiO-RGO hydrogel shows an average pore size at 18.3, 18.7, 20.4, 22.4, and 25.1 nm (inset to Fig. 4h) in the mesopore range. Taken together, these results indicate that the hydrogel consisted of a 3D porous interconnected architecture with random open pores and thin pore walls due to $V_4C_3T_x$@NiO and RGO. This is favorable for mitigating the aggregation and enhancing the electrical conductivity of $V_4C_3T_x$ MXenes and hence accessible active areas for practical applications.

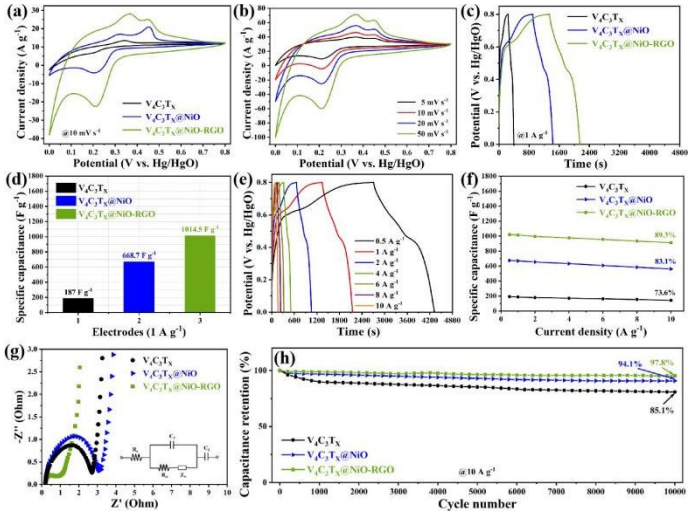

Fig. 5 Electrochemical performance of $V_4C_3T_x$, $V_4C_3T_x$@NiO, and $V_4C_3T_x$@NiO-RGO hydrogel in three-electrode system: (a) CV curves of $V_4C_3T_x$, $V_4C_3T_x$@NiO, and $V_4C_3T_x$@NiO-RGO hydrogel at the potential scan rate of 10 mV s^{-1}. (b) CV curves of $V_4C_3T_x$@NiO-RGO hydrogel at various scan rates. (c) GCD curves of $V_4C_3T_x$, $V_4C_3T_x$@NiO, and $V_4C_3T_x$@NiO-RGO hydrogel at the current density of 1 A g^{-1}. (d) the corresponding specific capacitance. (e) GCD curves of $V_4C_3T_x$@NiO-RGO hydrogel at various current densities. (f) Specific capacitance vs. current density plot of $V_4C_3T_x$, $V_4C_3T_x$@NiO, and $V_4C_3T_x$@NiO-RGO hydrogel. (g) Nyquist impedance plots of $V_4C_3T_x$, $V_4C_3T_x$@NiO, and $V_4C_3T_x$@NiO-RGO in a frequency range from 0.01 Hz to 100 k Hz (Inset is the the corresponding equivalent circuit diagram). (h) Cycling stability of $V_4C_3T_x$, $V_4C_3T_x$@NiO, and $V_4C_3T_x$@NiO-RGO hydrogel measured at 10 A g^{-1} for 10,000 cycles.

The capacitance characteristics of these samples were then tested by CV, GCD and EIS measurements within the potential range of 0 to 0.8 V (vs. Hg/HgO). Due to the high porosity and conductivity, and excellent mechanical strength, the $V_4C_3T_x$@NiO-RGO hydrogel can be used as a free-standing SC electrode, avoiding the complex traditional electrode fabrication process and the use of inactive binders and conductive additives. From Fig. 5a, one can clearly see that the $V_4C_3T_x$, $V_4C_3T_x$@NiO, and $V_4C_3T_x$@NiO-RGO electrodes all exhibited a pair of redox peaks at a scan rate of 10 mV s^{-1} in 1 M KOH, due to the variations of the V valence state in alkaline media. In comparison with $V_4C_3T_x$, $V_4C_3T_x$@NiO and $V_4C_3T_x$@NiO-RGO show slightly different anodic and cathodic peaks due to the reactions between Ni^{2+}/Ni^{3+} and Ti. More importantly, the $V_4C_3T_x$@NiO-RGO sample exhibited a far higher current density and larger integrated area, and hence a higher specific capacity, than $V_4C_3T_x$ and $V_4C_3T_x$@NiO. This demonstrates that the assembly of the 3D hydrogel structure indeed improves the pseudocapacitive performance of $V_4C_3T_x$@NiO-RGO. The CV curves of the $V_4C_3T_x$@NiO-RGO at various scan rates are shown in Fig. 5b. The reduction and oxidation peaks exhibited only a slight shift to the negative and positive directions with increasing scan rate, indicating reversible nature of the redox reactions.

To further evaluate the charge storage properties of these electrodes, the GCD curves were collected at the same current density of 1 A g^{-1} (Fig. 5c). These nonlinear GCD curves featured an evident plateau, consistent with the typical pseudocapacitive behavior and fast charge/discharge kinetics, in agreement with the CV results. In addition, the GCD curves show a nearly symmetric triangular-shaped shape, further confirming the reversible nature of the faradic redox reactions. Obviously, the $V_4C_3T_x$@NiO-RGO electrode exhibited a longer discharge time, and the specific capacitance (1021 F g^{-1}) was significantly higher than those of $V_4C_3T_x$@NiO (675 F g^{-1}) and $V_4C_3T_x$ (193 F g^{-1}) (Fig. 5d). The enhanced electrochemical performance is likely due to the gelation of $V_4C_3T_x$@NiO by a conducting 3D porous RGO framework. In fact, the specific capacity of $V_4C_3T_x$ is higher than the theoretically predicted capacity of $V_4C_3T_x$, which is due to the formation of vanadium oxide during the synthesis process that provides the additional pseudocapacitance. Similar phenomena have been observed in other MXenes.[15,16] As shown in Fig. 5e, there is an obvious IR drop in GCD measurements within the current density range of 0.5 to 10 A g^{-1}, indicating fast electron transfer and electrolyte ion diffusion in the device.

Usually, the specific capacitance of an electrode decreases as the discharge current density increases, because a large current density requires a quick charge/discharge reaction, as shown in Fig. 5f. Nevertheless, $V_4C_3T_x$@NiO-RGO can be seen to show an increase of the specific capacitance from 1021 F g^{-1} to 912 F g^{-1} as the current density varies from 0.5 to 10 A g^{-1}, indicating a high surface utilization and excellent rate performance (89.3% of the initial specific capacitance). As a comparison, the specific capacity of $V_4C_3T_x$ and $V_4C_3T_x$@NiO decreases from 193 to 142 F g^{-1} (73.6% retention) and 675 to 561.1 F g^{-1} (83.1% retention), respectively. In fact, the specific capacitance of the $V_4C_3T_x$@NiO-RGO electrode was superior to those of $Ti_3C_2T_x$-based electrodes reported previously, as displayed in Table S1.[44-56] The remarkable rate capability of $V_4C_3T_x$@NiO-RGO is attributed to the synergistic coupling effect among the structural components and the 3D architecture. Specifically, the conductive $V_4C_3T_x$ core in the heterostructure offers both abundant transport channels for ions and active interfacial centers, while the ultrathin NiO shells can increase the pseudocapacitance and promote the diffusion and migration of electrolyte ions. In addition, the 3D structure allow fast electrolyte ion diffusion and intimate contact of $V_4C_3T_x$@NiO with the electrolyte solution, leading to a high-rate capability.

To evaluate the electrical conductivity of the samples, EIS experiments were carried out in the range of 0.1 to 100 kHz. Fig. 5g depicts the Nyquist plots, with the equivalent circuit diagram

shown in the inset, where the semicircle in the high frequency region reflects the interfacial charge-transfer resistance (R_{ct}) and the linear part in the low frequency region is the Warburg resistance (W_d) due to diffusion of electrolyte species. It can be observed that the shape of the semicircle is similar for $V_4C_3T_x$, $V_4C_3T_x$@NiO, and $V_4C_3T_x$@NiO-RGO hydrogel. Yet, R_{ct} is obviously smaller for $V_4C_3T_x$@NiO-RGO hydrogel (2.8 Ω) than for $V_4C_3T_x$@NiO (5.1 Ω), indicative of enhanced electron-transfer kinetics. Additionally, the intercept (R_s) to the x-axis can be estimated to be 3.9 Ω for $V_4C_3T_x$@NiO and 1.8 Ω for $V_4C_3T_x$@NiO-RGO hydrogel, signifying that indeed the gelation of $V_4C_3T_x$@NiO enhanced the electrical conductivity. Notably, the slope of the linear segment for $V_4C_3T_x$@NiO-RGO hydrogel is greater than that of $V_4C_3T_x$@NiO, suggesting increasingly capacitive nature of the former.

Long-term cycle stability is another significant factor in practical applications, which was evaluated through consecutive charge-discharge process at the current density of 10 A g^{-1} for up to 10,000 cycles, and the results are depicted in Fig. 5h. It can be observed that more than 97.8% of the capacitance was retained (85.1% for $V_4C_3T_x$ and 94.1% for $V_4C_3T_x$@NiO) and the shape of GCD curves did not change appreciably, indicating a low leakage current and excellent long-term cyclic stability of the $V_4C_3T_x$@NiO-RGO electrode.

Structure and electrochemical characteristics of cathode materials

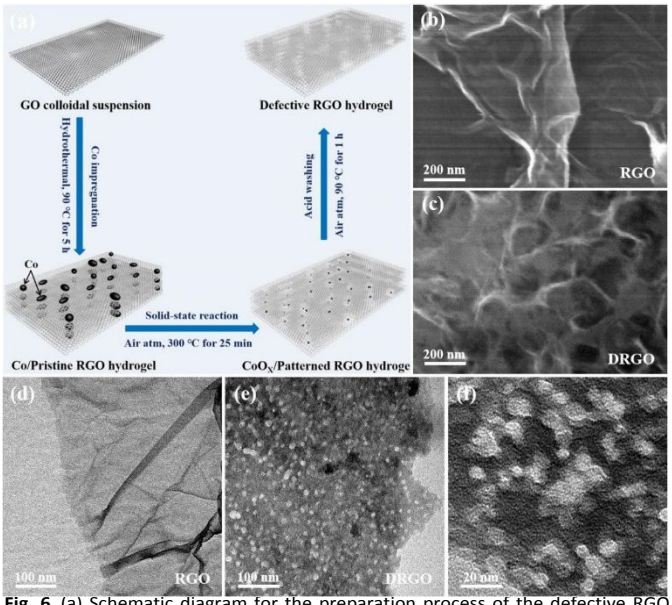

Fig. 6 (a) Schematic diagram for the preparation process of the defective RGO hydrogel. FESEM images of (b) RGO and (c) DRGO. TEM images of (d) RGO and (e) DRGO. Magnified TEM image (f) is collected from the region in (e).

Owing to the excellent electrical conductivity, large specific surface area and abundant mesoporous structure, defect-rich graphene has been considered as an ideal cathode material for ASCs. Herein, a DRGO hydrogel was prepared by a multi-step strategy as outlined in Fig. 6a. The microstructure of RGO and DRGO were first characterized by SEM measurements. The former can be seen to consist of almost transparent carbon nanosheets with a thin wrinkled structure (Fig. 6b), whereas the latter shows a well-defined porous structure (Fig. 6c). The average pore size of DRGO is about 25 nm and the pore distribution is rather uniform. The morphology was further analyzed by TEM measurements, where the samples showed a curled morphology consisting of a thin wrinkled paper-like structure. Before the patterning process (Fig. 6d), the exterior walls of RGO were cavity-free with an ordered graphitic structure; yet, after the cobalt-catalyzed gasification and acid digestion treatment, abundant mesopores were produced, as shown in Fig. 6e and 6f.

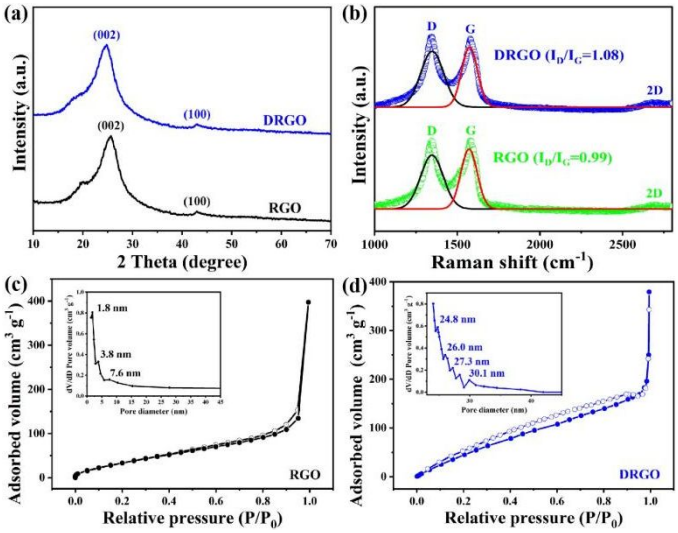

Fig. 7 (a) XRD patterns of RGO and DRGO. (b) Raman spectrum of RGO and DRGO. (c, d) N_2 adsorption-desorption isotherms of RGO and DRGO. Pore size distributions of RGO and DRGO in the insert.

The structural variations were also investigated by XRD and Raman spectroscopy measurements. From the XRD patterns in Fig. 7a, the diffraction peaks at 2θ = ca. 26° and 43° can be assigned to the (002) and (100) planes of carbon. The corresponding Raman spectra of RGO and DRGO are shown in Fig. 7b, where a pair of strong peaks can be identified, the G band at around 1587 cm^{-1} for the doubly degenerated zone center E_{2g} mode, and the D band at about 1352 cm^{-1} for the disordered sp^2 graphene.[57] Additionally, based on their fitting area, the D/G intensity ratio of DRGO (I_D/I_G = 1.08) is greater than that of RGO (I_D/I_G = 0.99), confirming a more defective structure of the former, where the structural defects likely arose from the Co-catalyzed cavity production.[58, 59]

The corresponding N_2 adsorption-desorption isotherms are displayed in Fig. 7c-d. RGO (Fig. 7c) can be seen to possess a type II isotherm, and shows the maximum adsorption capacity at P/P_0 = 1, suggestive of abundant micropores in the sample. For comparison, DRGO exhibits a type IV isotherm with a significant hysteresis loop within the relative pressure of 0.1 to 1.0, due to the formation of a mesoporous structure. The porosity can be further examined by the BJH method. From the inset to Fig. 7c, RGO can be seen to display a broad distribution of pore sizes, and the average pore sizes are located at 1.8, 3.8 and 7.6 nm, indicating that the sample consisted mainly of micropores. For DRGO, the main pore sizes are 24.8, 26.0, 27.3 and 30.1 nm, consistent with the mesoporous structure (inset to Fig. 7d). The specific BET surface area of DRGO is estimated to be 586 $m^2 g^{-1}$, markedly higher than that (189 $m^2 g^{-1}$) of pristine RGO.

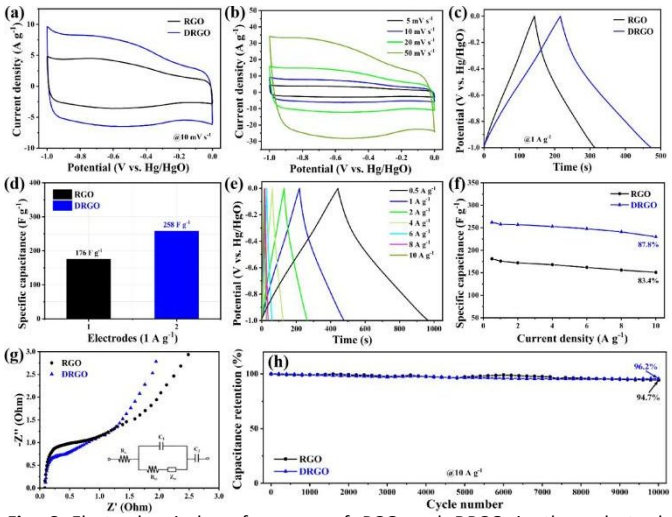

Fig. 8 Electrochemical performance of RGO and DRGO in three-electrode configuration: (a) CV curves of RGO and DRGO at the potential scan rate of 10 mV s^{-1}. (b) CV curves of DRGO at various scan rates. (c) GCD curves of RGO and DRGO at the current density of 1 A g^{-1}. (d) The corresponding specific capacitance. (e) GCD curves of DRGO at various current densities. (f) Specific capacitance vs. current density plot of RGO and DRGO. (g) Nyquist impedance plots of RGO and DRGO in a frequency range from 0.01 Hz to 100 k Hz (Inset is the corresponding equivalent circuit diagram). (h) Cycling stability of RGO and DRGO measured at 10 A g^{-1} for 10,000 cycles.

The electrochemical performance of these samples was then examined within the potential range of -1 to 0 V in a 1 M KOH electrolyte. Fig. 8a displays the CV curves of RGO and DRGO hydrogel electrodes at the scan rate of 10 mV s^{-1}. All CV curves are quasi-rectangular in shape, and the CV curve of the DRGO hydrogel electrode shows a larger integration area than the RGO hydrogel electrode, revealing a higher specific capacitance and faster charge/discharge property for power storage. Fig. 8b shows the CV curves of the DRGO hydrogel electrode at different scan rates. All the CV curves exhibit a rectangular shape and there is no significant distortion with increasing potential scan rates, indicating excellent rate stability and low series resistance. The capacitance characteristics of these electrodes were further evaluated by GCD measurements at the same current density of 1 A g^{-1}. As shown in Fig. 8c, the DRGO hydrogel electrode exhibits a longer discharge time, and the specific capacitance (258 F g^{-1}) was indeed higher than that (176 F g^{-1}) of the RGO hydrogel electrode (Fig. 8d). This suggests enhanced charge storage property with the introduction of defect by a Co catalyzed gasification method, in good agreement with the CV results. From Fig. 8e, there is no apparent IR drop in the GCD curves of the DRGO hydrogel electrode within the current density range of 0.5 to 10 A g^{-1}, indicating perfect capacitive behavior and low internal resistance of the device. Additionally, the GCD curves were all symmetric, indicative of good charge-discharge stability. Both the CV and GCD curves suggest reversible EDLC behavior of the DRGO hydrogel.

Fig. 8f depicts the specific capacitances of RGO and DRGO hydrogel electrodes at different current densities, which decreased with the increase of the discharge current densities. The DRGO hydrogel electrode features a specific capacitance of 262 F g^{-1} at 0.5 A g^{-1}, and 230 F g^{-1} at 10 A g^{-1} (87.8% retention), as compared to 181 and 151 F g^{-1} for the RGO hydrogel electrode (83.4% retention). This suggests better rate stability of the DRGO hydrogel electrode, due to the small charge-transfer resistance. Notably, the electrochemical performance of this 3D DRGO hydrogel electrode is better than most of the results of relevant carbon-based materials for SC applications reported previously (Table S2).[60-70] The excellent performance can be attributed to the appropriate pore structure, and good electrical conductivity. Firstly, the high porosity of the samples greatly increases the electrode/electrolyte contact area. Secondly, the porous structure offers a large volume energy density. Thirdly, the porous structure provides vast pathways for ion transport and high-rate performance.

Note that the electrical conductivity of the DRGO hydrogel was retained despite the formation of the defect structure. From the Nyquist plots in Fig. 8g and the equivalent circuit diagram in the inset, it can be observed that the R_{ct} of DRGO hydrogel (2.3 Ω) is similar to that of the RGO hydrogel (2.2 Ω), whereas the slope of the linear segment in the DRGO hydrogel is greater than that of the RGO hydrogel, consistent with the better capacitive performance of the DRGO hydrogel. Moreover, this method indicates that only carbon in contact with metallic and oxide particles will be oxidized by the solid-state reaction at a relatively low temperature (300 °C), which retains the planar sp^2 carbon sheets and high electrical conductivity. The cycling performance of RGO and DRGO hydrogel electrodes was then tested by a consecutive charge-discharge process at 10 A g^{-1} (Fig. 8h). After 10,000 cycles, the capacitance of the DRGO hydrogel still retains 96.2% of the initial value, while only about 94.7% for the RGO hydrogel, indicating a much better stability of the DRGO hydrogel.

Electrochemical properties of $V_4C_3T_X$@NiO-RGO//DRGO ASC

In order to evaluate the potential applications of the prepared materials as electrodes for energy-storage devices, a free-standing $V_4C_3T_X$@NiO-RGO//DRGO ASC device (Fig. 9a) was constructed by using the $V_4C_3T_X$@NiO-RGO hydrogel as the anode, DRGO hydrogel as the cathode, and 1 KOH as the electrolyte, with a porous polymer membrane as the separator. To optimize the performance of this ASC device, the mass ratio of the anode to cathode was adjusted to approximately 1:3.2 (with the total mass loading of the active materials at 4.2 mg), according to charge balance theory.[3, 8, 42] As shown in Fig. 9b, the CV curves were firstly measured at a scan rate of 10 mV s^{-1} and displayed a stable voltage window and from 0 to 0.8 V for $V_4C_3T_X$@NiO-RGO and from -1 to 0 V for DRGO electrodes, which determine the operating voltage of the ASC device. Fig. 9c displays the CV curves of the ASC device within various voltage ranges (0 ~ 1.4, 0 ~ 1.5, 0 ~ 1.6, 0 ~ 1.7, 0 ~ 1.8, and 0 ~ 1.9 V) at a scan rate of 50 mV s^{-1}. Notably, the stable voltage can be enlarged to 1.8 V. A clear sharp current increase in the red circle can be observed due to obvious oxygen evolution with the operating voltage further increased to 1.9 V. To maximize the cycle life, we set the operating voltage of the ASC device at 1.8 V. Fig. 9d shows the typical CV curves of the $V_4C_3T_X$@NiO-RGO//DRGO ASC at different scan rates, where a pair of well-defined anodic and cathodic peaks are observed corresponding to the pseudocapacitve behavior of the reversible redox reactions between Ni^{2+}/Ni^{3+} and Ti, indicating that the dominant

charge storage mechanism is Faradaic with a suitable operating potential window of 1.8 V.

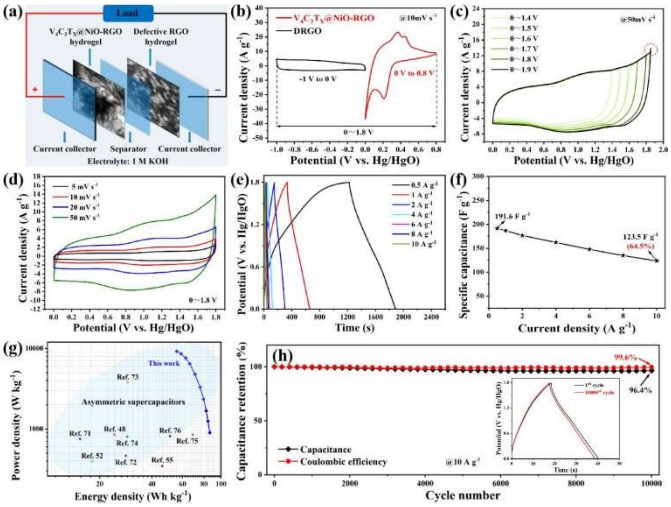

Fig. 9 Electrochemical performance of the $V_4C_3T_X$@NiO-RGO//DRGO ASC device: (a) Schematic diagram for the construction of the assembled ASC device. (b) CV curves of individual $V_4C_3T_X$@NiO-RGO positive and DRGO negative electrodes measured in a three-electrode system at a scan rate of 10 mV s^{-1}. (c) CV curves of the ASC at 50 mV s^{-1} with different potential windows. (d) CV curves of the ASC at different scan rates at 0~1.8 V. (e) GCD curves of the ASC at different current densities at 0~1.8 V. (f) Specific capacitances calculated form the GCD curves at various current densities. (g) Ragone plots of our ASC device compared to other $Ti_3C_2T_X$-based ASCs reported in the literature. (h) Cycling and Coulmbic efficiency at 10 A g^{-1} (inset shows the 1 rd and 10000 rd cycle GCD curves during the cycling test).

Additionally, the shape of the CV curves remained almost unchanged with increasing sweep rate, suggesting an excellent rate capability and capacitive behavior of the ASC device. GCD curves at various current densities in Fig. 9e display a curvature at similar voltages as the CVs, which originates from the pseudocapacitive nature of the electrode materials. Moreover, the symmetric triangular shape with no clear IR drop of the GCD curves once again confirms the excellent capacitive behaviors and electrochemical reversibility of the ASC device. The specific capacitance of the ASC device at different current density can be calculated according to the GCD curves, and the capacitance of this ASC is estimated to be 191.6 and 123.5 F g^{-1} at 0.5 and 10 A g^{-1}, respectively (Fig. 9f). Rate capability at the high current density of 10.0 A g^{-1} is 64.5% of its initial value. This high-rate performance can be attributed not only to capacity matching, but also to kinetic balance and fast redox kinetics of both electrodes. Furthermore, the ASC device provides an ultrahigh energy density of 86.22 W h kg^{-1} at a power density of 900 W kg^{-1}. Even at a high power density of 9240 W kg^{-1}, an energy density of 55.58 Wh kg^{-1} was retained. Such a performance is superior to those of Ni- and $V_4C_3T_X$-based ASCs reported previously, as shown in the Ragone plot (Fig. 9g).[48, 52, 55, 71-76]

Consecutive GCD measurements at a current density of 10 A g^{-1} for 10,000 cycles were then carried out to evaluate the cycling stability. From Fig. 9h, this ASC device can be seen to retain 96.4% of its initial capacitance over 10,000 cycles, with virtually no change of the GCD curves (inset to Fig. 9h), indicating remarkable cycling stability.In fact, the cycle life of our ASC is comparable to that of previously reported similar ASCs.[77-80] Additionally, the Coulombic efficiency was stable at near 99.6% throughout the cycle test (Fig. 9h), further manifesting that our ASC device has excellent energy conversion efficiency.

4. Conclusions

In summary, 3D $V_4C_3T_X$@NiO-RGO heterostructured hydrogel was synthesized by an efficient two-step process. High-pseudocapacitance NiO nanosheets were uniformly deposited on the surface of highly conductive $V_4C_3T_X$ constructing a face-to-face contact framework. Additionally, the 3D interconnected architecture significantly avoided the self-restacking of the $V_4C_3T_X$@NiO-RGO, resulting in a favorable electrochemical performance with an ultrahigh specific capacitance of 1021 F g^{-1} at 0.5 A g^{-1} and an excellent rate capability (89.3% at 10 A g^{-1}). Both the heterostructure and 3D hydrogel configurations were key to the high energy density and power density of the electrode. The 3D DRGO hydrogel was prepared through a cost-effective hydrothermal followed by cobalt-catalyzed gasification. Due to the abundant mesopore structure arising from defect engineering and the 3D framework, the DRGO hydrogel delivered a high specific capacitance of 262 F g^{-1} at 0.5 A g^{-1}. With these two materials as the anode and cathode, a free-standing $V_4C_3T_X$@NiO-RGO//DRGO ASC device was assembled, featuring an expanded voltage window of 1.8 V, a maximum energy density of 86.22 Wh kg^{-1} at 900 W kg^{-1} (even retains 55.58 Wh kg^{-1} at 9240 W kg^{-1}), and an outstanding cycling performance with a capacitance retention up to 96.4% over 10,000 cycles at 10 A g^{-1}. Results from this work paves an efficient way to the synthesis of MXene-based heterostructured hydrogels for high-energy density free-standing ASCs.

Supporting Information

Supporting information is available from The Royal Society of Chemistry Online Library or from the author.

Author Contributions

Yuqin Tian and Weiwen Chen contributed equally. The manuscript was written through contributions of all authors. All authors have given approval to the final version of the manuscript.

Acknowledgements

This work was supported by the National Natural Science Foundation of China (Grant No. 52073022, and 31961133017), and the National Basic Research Program of China (Grant No.5 2014CB745100). S. W. C. thanks the National Science Foundation (CHE-1900235) for partial support of the work.

Conflicts of Interest

There are no conflicts of interest to declare.

References

1 L. Marti and R. Puertas, *Sustain Technol Entrepreneurship*, **2022**, 1, 100007. DOI:10.1016/j.stae.2022.100007
2 B. Nastasi, N. Markovska, T. Puksec, N. Duić and A. Foley, *Renew Sustain Energy Rev*, **2022**, 157, 112071. DOI: 10.1016/j.rser.2022.112071
3 W. Liang and I. Zhitomirsky, *Electrochim Acta*, **2022**, 406, 139843. DOI:10.1016/j.electacta.2022.139843
4 D. P. Chatterjee and A. K. Nandi, *J Mater Chem A*, **2021**, 9, 15880-15918. DOI: 10.1039/d1ta02505h
5 H. Qin, P. Liu, C. Chen, H. P. Cong and S. H. Yu, *Nat Commun*, **2021**, 12, 4297. DOI: 10.1038/s41467-021-24568-w
6 H. Ma, H. Chen, Y. Hu, B. Yang, J. Feng, Y. Xu, Y. Sun, H. Cheng, C. Li, X. Yan and L. Qu, *Energy Environ Sci*, **2022**, 15, 1131-1143. DOI: 10.1039/d1ee03672f
7 H. Banda, J. H. Dou, T. Chen, N. J. Libretto, M. Chaudhary, G. M. Bernard, J. T. Miller, V. K. Michaelis and M. Dinca, *J Am Chem Soc*, **2021**, 143, 2285-2292. DOI: 10.1021/jacs.0c10849
8 [8] Y. Shao, M. F. El-Kady, J. Sun, Y. Li, Q. Zhang, M. Zhu, H. Wang, B. Dunn and R. B. Kaner, *Chem Rev*, **2018**, 118, 9233-9280. DOI: 10.1021/acs.chemrev.8b00252
9 R. Reece, C. Lekakou and P. A. Smith, *ACS Appl Mater Interfaces*, **2020**, 12, 25683-25692. DOI: 10.1021/acsami.9b23427
10 D. S. Charles, F. Guo, X. Shan, S. Kim, Z. W. Lebens-Higgins, W. Xu, D. Su, L. F. J. Piper and X. Teng, *J Mater Chem A*, **2021**, 9, 15629-15636. DOI: 10.1039/d1ta02003j
11 J. Zhao and A. F. Burke, *J Energy Chem*, **2021**, 59, 276-291. DOI: 10.1016/j.jechem.2020.11.013
12 Y. Zhang, H.-x. Mei, Y. Cao, X.-h. Yan, J. Yan, H.-l. Gao, H.-w. Luo, S.-w. Wang, X.-d. Jia, L. Kachalova, J. Yang, S.-c. Xue, C.-g. Zhou, L.-x. Wang and Y.-h. Gui, *Coord Chem Rev*, **2021**, 438, 213910. DOI: 10.1016/j.ccr.2021.213910
13 J. Pang, R. G. Mendes, A. Bachmatiuk, L. Zhao, H. Q. Ta, T. Gemming, H. Liu, Z. Liu and M. H. Rummeli, *Chem Soc Rev*, **2019**, 48, 72-133. DOI: 10.1039/c8cs00324f
14 M. Naguib, M. Kurtoglu, V. Presser, J. Lu, J. Niu, M. Heon, L. Hultman, Y. Gogotsi and M. W. Barsoum, *Adv Mater*, **2011**, 23, 4248-4253. DOI: 10.1002/adma.201102306
15 M. R. Lukatskaya, S. Kota, Z. Lin, M.-Q. Zhao, N. Shpigel, M. D. Levi, J. Halim, P.-L. Taberna, M. W. Barsoum, P. Simon and Y. Gogotsi, *Nature Energy*, **2017**, 2, 17105. DOI: 10.1038/nenergy.2017.105
16 M. Ghidiu, M. R. Lukatskaya, M. Q. Zhao, Y. Gogotsi and M. W. Barsoum, *Nature*, **2014**, 516, 78-81. DOI: 10.1038/nature13970
17 Y. Gogotsi and B. Anasori, *ACS Nano*, **2019**, 13, 8491-8494. DOI: 10.1021/acsnano.9b06394
18 B. Anasori, M. R. Lukatskaya and Y. Gogotsi, *Nat Rev Materials*, **2017**, 2, 1-17. DOI: 10.1038/natrevmats.2016.98
19 J. Zhao, Q. Li, T. X. Shang, F. F. Wang, J. Zhang, C. N. Geng, Z. T. Wu, Y. Q. Deng, W. C. Zhang, Y. Tao, Q. H. Yang, *Nano Energy*, **2021**, 86, 106091. DOI: 10.1016/j.nanoen.2021.106091
20 M. H. Tran, T. Schäfer, A. Shahraei, M. Dürrschnabel, L. Molina-Luna, U. I. Kramm and C. S. Birkel, *ACS Appl Energy Mater*, **2018**, 1, 3908-3914. DOI: 10.1021/acsaem.8b00652
21 X. Wang, S. Lin, H. Tong, Y. Huang, P. Tong, B. Zhao, J. Dai, C. Liang, H. Wang, X. Zhu, Y. Sun and S. Dou, *Electrochim Acta*, **2019**, 307, 414-421. DOI: 10.1016/j.electacta.2019.03.205
22 J. Zhou, S. Lin, Y. Huang, P. Tong, B. Zhao, X. Zhu and Y. Sun, *Chem Eng J*, **2019**, 373, 203-212. DOI: 10.1016/j.cej.2019.05.037
23 H. Li, X. Wang, H. Li, S. Lin, B. Zhao, J. Dai, W. Song, X. Zhu and Y. Sun, *J Alloys Compd*, **2019**, 784, 923-930. DOI: 10.1016/j.jallcom.2019.01.111
24 H. Huang, J. Cui, G. Liu, R. Bi and L. Zhang, *ACS Nano*, **2019**, 13, 3448-3456. DOI: 10.1021/acsnano.8b09548
25 H. Lei, S. Z. Tan, L. J. Ma, Y. Z. Liu, Y. Y. Liang, M. S. Javed, Z. L. Wang, Z. L. Zhu, and W. J. Mai, ACS Appl Mater Interfaces, **2020**, 12, 44639-44647. DOI: 10.1021/acsami.0c11185
26 X. Wang, H. Li, H. Li, S. Lin, J. Bai, J. Dai, C. Liang, X. Zhu, Y. Sun and S. Dou, *J Mater Chem A*, **2019**, 7, 2291-2300. DOI: 10.1039/c8ta11249e
27 J. Xu, L. Wu, Y. Liu, J. Zhang, J. Liu, S. Shu, X. Kang, Q. Song, D. Liu, F. Huang and Y. Hu, *Surf Interfaces*, **2020**, 18, 100420. DOI: 10.1016/j.surfin.2019.100420
28 K. Li, M. Liang, H. Wang, X. Wang, Y. Huang, J. Coelho, S. Pinilla, Y. Zhang, F. Qi, V. Nicolosi and Y. Xu, *Adv Funct Mater*, **2020**, 30, 2000842. DOI: 10.1002/adfm.202000842
29 Y. Ma, Y. Yue, H. Zhang, F. Cheng, W. Zhao, J. Rao, S. Luo, J. Wang, X. Jiang, Z. Liu, N. Liu and Y. Gao, *ACS Nano*, **2018**, 12, 3209-3216. DOI: 10.1021/acsnano.7b06909
30 Y. Z. Zhang, J. K. El-Demellawi, Q. Jiang, G. Ge, H. Liang, K. Lee, X. Dong and H. N. Alshareef, *Chem Soc Rev*, **2020**, 49, 7229-7251. DOI: 10.1039/d0cs00022a
31 H. Hu, Z. Zhao, W. Wan, Y. Gogotsi and J. Qiu, *Adv Mater*, **2013**, 25, 2219-2223. DOI: 10.1002/adma.201204530
32 Y. Chen, X. Xie, X. Xin, Z. R. Tang and Y. J. Xu, *ACS Nano*, **2019**, 13, 295-304. DOI: 10.1021/acsnano.8b06136
33 Y. Deng, T. Shang, Z. Wu, Y. Tao, C. Luo, J. Liang, D. Han, R. Lyu, C. Qi, W. Lv, F. Kang and Q. H. Yang, *Adv Mater*, **2019**, 31, 1902432. DOI: 10.1002/adma.201902432
34 M. D. Stoller and R. S. Ruoff, *Energy Environ Sci*, **2010**, 3, 1294-1301. DOI: 10.1039/c0ee00074d
35 C. N. Rao, A. K. Sood, K. S. Subrahmanyam and A. Govindaraj, *Angew Chem Int Ed Engl*, **2009**, 48, 7752-7777. DOI: 10.1002/anie.200901678
36 B. Liu, H. Shioyama, H. Jiang, X. Zhang and Q. Xu, *Carbon*, **2010**, 48, 456-463. DOI: 10.1016/j.carbon.2009.09.061
37 N. L. Torad, M. Hu, Y. Kamachi, K. Takai, M. Imura, M. Naito and Y. Yamauchi, *Chem Commun (Camb)*, **2013**, 49, 2521-2523. DOI: 10.1039/c3cc38955c
38 Z. Chen, Y.-M. Lin, M. J. Rooks and P. Avouris, *Phys E*, **2007**, 40, 228-232. DOI: 10.1016/j.physe.2007.06.020
39 S. Pang, H. N. Tsao, X. Feng and K. Müllen, *Adv Mater*, **2009**, 21, 3488-3491. DOI: 10.1002/adma.200803812
40 H. Bai, C. Li, X. Wang and G. Shi, *J Phys Chem C*, **2011**, 115, 5545-5551. DOI: 10.1021/jp1120299
41 S. Stankovich, D. A. Dikin, G. H. B. Dommett, K. M. Kohlhaas, E. J. Zimney, E. A. Stach, R. D. Piner, S. T. Nguyen and R. S. Ruoff, *Nature*, **2006**, 442, 282-286. DOI: 10.1038/nature04969
42 R. S. Devan, R. A. Patil, J.-H. Lin and Y.-R. Ma, *Adv Funct Mater*, **2012**, 22, 3326-3370. DOI: 10.1002/adfm.201201008
43 Z. Yang, F. Xu, W. Zhang, Z. Mei, B. Pei and X. Zhu, *J Power Sources*, **2014**, 246, 24-31. DOI: 10.1016/j.jpowsour.2013.07.057
44 W. Chen, D. Zhang, K. Yang, M. Luo, P. Yang and X. Zhou, *Chem Eng J*, **2021**, 413, 127524. DOI: 10.1016/j.cej.2020.127524
45 Z. Pan and X. Ji, *J Power Sources*, **2019**, 439, 227068. DOI: 10.1016/j.jpowsour.2019.227068
46 C. Liu, Y. Bai, W. Li, F. Yang, G. Zhang and H. Pang, *Angew Chem Int Ed Engl*, **2022**, 61, e202116282. DOI: 10.1002/ange.202116282
47 X. Wang, H. Li, H. Li, S. Lin, W. Ding, X. Zhu, Z. Sheng, H. Wang, X. Zhu and Y. Sun, *Adv Funct Mater*, **2020**, 30, 0190302. DOI: 10.1002/adfm.201910302
48 X. Chen, Y. Liu, Q. Zhou and F. Su, *ChemistrySelect*, **2020**, 5, 14768-14775. DOI: 10.1002/slct.202004181
49 D. Wei, W. Wu, J. Zhu, C. Wang, C. Zhao and L. Wang, *J Electroanal Chem*, **2020**, 877, 114538. DOI: 10.1016/j.jelechem.2020.114538
50 W. Wu, D. Niu, J. Zhu, Y. Gao, D. Wei, C. Zhao, C. Wang, F. Wang, L. Wang and L. Yang, *Cer Int*, **2019**, 45, 16261-16269. DOI: 10.1016/j.ceramint.2019.05.149

51 J. Li, X. Yuan, C. Lin, Y. Yang, L. Xu, X. Du, J. Xie, J. Lin and J. Sun, *Adv Energy Mater*, **2017**, 7, 1-6. DOI: 10.1002/aenm.201602725

52 J. Guo, Y. Zhao, A. liu and T. Ma, *Electrochim Acta*, **2019**, 305, 164-174. DOI: 10.1016/j.electacta.2019.03.025

53 J. Yan, C. E. Ren, K. Maleski, C. B. Hatter, B. Anasori, P. Urbankowski, A. Sarycheva and Y. Gogotsi, *Adv Funct Mater*, **2017**, 27, 1701264. DOI: 10.1002/adfm.201701264

54 J. Song, P. Hu, Y. Liu, W. Song and X. Wu, *ChemistrySelect*, **2019**, 4, 12886-12890. DOI: 10.1002/slct.201903511

55 R. Zhao, M. Wang, D. Zhao, H. Li, C. Wang and L. Yin, *ACS Energy Lett*, **2017**, 3, 132-140. DOI: 10.1021/acsenergylett.7b01063

56 W. Chen, Y. Peng, Z. Qiu, X. Zhang and H. Xu, *J Alloys Compd*, **2022**, 901, 163614. DOI: 10.1016/j.jallcom.2022.163614

57 A. C. Ferrari, J. C. Meyer, V. Scardaci, C. Casiraghi, M. Lazzeri, F. Mauri, S. Piscanec, D. Jiang, K. S. Novoselov, S. Roth and A. K. Geim, *Phys Rev Lett*, **2006**, 97, 187401. DOI: 10.1103/PhysRevLett.97.187401

58 H.-W. Wang, Z.-A. Hu, Y.-Q. Chang, Y.-L. Chen, H.-Y. Wu, Z.-Y. Zhang and Y.-Y. Yang, J Mater Chem, **2011**, 21, 10504-10511. DOI: 10.1039/c1jm10758e

59 Y. Tao, W. Liu, Z. Li, Y. Zheng, X. Zhu,H. Wang, Y. Wang, Q. Lin, Q. Wu, Y. Pang, Z. Shen and H. Chen, Journal of Colloid and Interface Science, **2021**, 602 , 636-645. DOI:10.1016/j.jcis.2021.06.060

60 K. H. Lee, J. Oh, J. G. Son, H. Kim and S. S. Lee, ACS Appl Mater Interfaces, 2014, 6, 6361-6368. DOI: 10.1021/am405735c

61 B. Zheng, T.-W. Chen, F.-N. Xiao, W.-J. Bao and X.-H. Xia, *J Solid State Electrochem*, **2013**, 17, 1809-1814. DOI: 10.1007/s10008-013-2101-8

62 P. Wen, P. Gong, Y. Mi, J. Wang and S. Yang, *RSC Adv*, **2014**, 4, 35914-35918. DOI: 10.1039/c4ra04788e

63 M. Benedetti, C. R. Girelli, D. Antonucci, S. A. De Pascali and F. P. Fanizzi, *Inorg Chim Acta*, **2014**, 413, 109-114. DOI: 10.1016/j.ica.2013.12.044

64 J. Guo, X. Xu, J. P. Hill, L. Wang, J. Dang, Y. Kang, Y. Li, W. Guan and Y. Yamauchi, *Chem Sci*, **2021**,12,10334-10340. DOI: 10.1039/d1sc00915j

65 Y. Lv, L. Gan, M. Liu, W. Xiong, Z. Xu, D. Zhu and D. S. Wright, *J Power Sources*, **2012**, 209, 152-157. DOI: 10.1016/j.jpowsour.2012.02.089

66 B. Qiu, C. Pan, W. Qian, Y. Peng, L. Qiu and F. Yan, *Journal of Mater Chem A*, **2013**, 1, 6373-6378. DOI: 10.1039/c3ta10774d

67 H. Zhao, L. Wang, D. Jia, W. Xia, J. Li and Z. Guo, *J. Mater. Chem. A*, **2014**, 2, 9338-9344. DOI: 10.1039/c4ta00069b

68 T.-X. Shang, M.-Y. Zhang and X.-J. Jin, *RSC Adv.*, **2014**, 4, 39037-39044. DOI: 10.1039/c4ra05881j

69 X. Yang, X. Zhuang, Y. Huang, J. Jiang, H. Tian, D. Wu, F. Zhang, Y. Mai and X. Feng, *Polym Chem*, **2015**, 6, 1088-1095. DOI: 10.1039/c4py01408a

70 H. Yi, H. Wang, Y. Jing, T. Peng and X. Wang, *J Power Sources*, **2015**, 285, 281-290. DOI: 10.1016/j.jpowsour.2015.03.106

71 Z. Pan, F. Cao, X. Hu and X. Ji, *J Mater Chem A*, **2019**, 7, 8984-8992. DOI: 10.1039/c9ta00085b

72 K. O. Oyedotun, D. Y. Momodu, M. Naguib, A. A. Mirghni, T. M. Masikhwa, A. A. Khaleed, M. Kebede and N. Manyala, *Electrochim Acta*, **2019**, 301, 487-499. DOI: 10.1016/j.electacta.2019.01.158

73 Q. Jiang, N. Kurra, M. Alhabeb, Y. Gogotsi and H. N. Alshareef, *Adv Energy Mater*, **2018**, 8, 1703043. DOI: 10.1002/aenm.201703043

74 H. Liu, R. Hu, J. Qi, Y. Sui, Y. He, Q. Meng, F. Wei, Y. Ren, Y. Zhao and W. Wei, *Adv Mater Interfaces*, **2020**, 7, 1901659. DOI: 10.1002/admi.201901659

75 J. Fu, L. Li, J. M. Yun, D. Lee, B. K. Ryu and K. H. Kim, *Chemical Engineering Journal*, **2019**, 375, 121939. DOI: 10.1016/j.cej.2019.121939

76 J. V. Vaghasiya, C. C. Mayorga-Martinez, J. Vyskočil, Z. Sofer and M. Pumera, *Adv Funct Mater*, **2020**, 30, 2003673. DOI: 10.1002/adfm.202003673

77 J. Zhu, C. Han, X. Song, Materials Chemistry and Physics, **2022**,283,126038.DOI: 10.1016/j.matchemphys.2022.126038

78 Y. Wu, H. Chen, Y. Lu, J. Yang, X. Zhu, Y. Zheng, G. Lou, Y. Wu, Q. Wu, Z. Shen, Z. Pan, Journal of Colloid And Interface Science, **2021**, 581, 455-464. DOI: 10.1016/j.jcis.2020.08.013

79 Y. Tao, Y. Wu, H. Chen, W. Chen, J. Wang, Y. Tong, G. Pei, Z. Shen, C. Guan, Chemical Engineering Journal, **2020**, 396, 125364. DOI: 10.1016/j.cej.2020.125364

80 C. Su, S. Xu, L. Zhang, X. Chen, G. Guan, N. Hu, Y. Su, Z. Zhou, H. Wei, Z. Yang, Y. Qin, Electrochimica Acta, **2019**, 305,81-89. DOI: 10.1016/j.electacta.2019.03.013